International Journal of Fracture **86:** 5–36, 1997.

Some recent developments in computational modelling of concrete fracture

RENÉ DE BORST*
Delft University of Technology, Faculty of Civil Engineering, P.O. Box 5048, NL-2600 GA Delft. The Netherlands

Received 27 August 1996; accepted in revised form 10 February 1997

Abstract. Some of the most important aspects of numerical modelling of cracking in concrete are reviewed. After a discussion of the three main lines in modelling cracking – discrete crack models, smeared representations and approaches using lattice models – a concise treatment including comparative studies is given of the various smeared crack approaches that exist to date. Next a discussion is presented of some issues pertaining to the sensitivity of numerical results on the fineness of the mesh and the direction of the mesh lines, and on size effects in concrete structures.

Key words: Concrete fracture, smeared-crack models, damage mechanics, localization, mesh sensitivity, finite element analysis.

1. Introduction

Numerical modelling of cracking in concrete started in the late 1960s with the landmark papers of Ngo and Scordelis (1967) and Rashid (1968), in which the discrete and smeared crack models were introduced. Especially the latter approach gained much popularity, and in the 1970s comprehensive efforts were invested in developing constitutive models in a smeared setting which could reproduce the experimentally observed stress-strain characteristics of concrete. Much attention was devoted to modelling the behaviour of concrete under triaxial compressive stress conditions. This is somewhat surprising, since the majority of the nonlinearity of concrete is caused by cracking, a phenomenon that is primarily due to the limited capacity of concrete to sustain tensile stresses (or perhaps better, tensile strains), and because in the vast majority of the applications of concrete there exists a state of plane stress. It may be that the research in constitutive modelling of soils is partly responsible for the strong emphasis on triaxial stress states. Also, the by then importance of the nuclear industry, which is one of the rare applications of concrete where thick-walled structures are commonplace, may have promoted this focus of research. Typically, nonlinear elastic models and plasticity-based models were employed to model the response characteristics. With respect to cracking, the two major modifications that were introduced were the so-called shear retention factor (Suidan and Schnobrich, 1973), and the replacement of the sudden stress drop upon crack initiation by a descending branch in the tensile stress-strain relation to represent the contribution of the stiffness of the conrete between the cracks in reinforced concrete, a phenomenon that is now commonly denoted as *tension-stiffening*.

In the early 1980s we witnessed a number of most important novel developments. Firstly, there was the recognition, originally by Cope et al. (1980), that the introduction of a shear retention factor causes the principal stresses in a cracked integration point to rotate upon

* Also at: Eindhoven University of Technology, Faculty of Mechanical Engineering

further loading. Moreover, in combination with a descending branch in the tensile stress-strain diagram, the major tensile stress may easily exceed the tensile strength in another direction than the one normal to the crack if the crack direction is fixed upon crack initiation. Without the use of a shear retention factor this cannot happen, and the importance of this phenomenon has initially been overlooked when the shear retention factor was introduced.

Another most important issue was the recognition that plain concrete is not a perfectly brittle material in the Griffith sense, but that it has some residual load-carrying capacity after reaching the tensile strength. This experimental observation led to the replacement of purely brittle crack models by *tension-softening* models, in which a descending branch was introduced to model the gradually diminishing tensile strength of concrete upon further crack opening. Of course, this effect also exists in reinforced concrete and much confusion has existed since then about how to model tension-softening and tension-stiffening in reinforced concrete in a rational manner.

The introduction of softening in the cracking models was also motivated on theoretical grounds. It was observed that the use of strength models (Cedolin and Bažant, 1980) or the straightforward use of strain-softening models leads to an unacceptable and unphysical mesh sensitivity (Bažant, 1976; Crisfield, 1982). A similar observation had been made for discrete crack models, and probably motivated by the Dugdale–Barenblatt cohesive crack models (Barenblatt, 1962; Dugdale, 1960), Hillerborg published as early as in 1976 his landmark paper in which he introduced the Fictitious Crack Model (Hillerborg et al., 1976), which ensured a mesh-independent energy release upon crack propagation. Adapting this concept to smeared formulations, Bažant and Oh (1983) developed the Crack Band Model, in which the fracture energy introduced by Hillerborg was smeared out over the width of area in which the crack *localises*, for lower-order elements typically equal to the width of one element.

Shortly after the introduction of the Crack Band Model, it was recognised that this model can yield reasonable solutions from an engineering point of view, but that it does not resolve the fundamental difficulty that is a consequence of the use of strain-softening stress-strain relations, namely that the governing partial differential equations can locally change type. As a result the rate boundary value problem becomes ill-posed. The observed mesh sensitivity in numerical simulations is a mere manifestation of this mathematical deficiency of smeared-crack models. To overcome this essential shortcoming, a number of models have been put forward, ranging from fully nonlocal models (Bažant et al., 1984; Pijaudier-Cabot and Bažant, 1987), via gradient approaches (Aifantis, 1984; Schreyer and Chen, 1986; Lasry and Belytschko, 1988; Mühlhaus and Aifantis, 1991; de Borst and Mühlhaus, 1992; Pamin, 1994), to Cosserat models (Mühlhaus and Vardoulakis, 1987; de Borst, 1991; de Borst, 1993) and, for the case of transient loadings, the rate-dependent models (Sluys, 1992). For an overview the reader is referred to de Borst et al. (1993).

In this contribution we shall focus on the topics that surfaced in the 1980s and have become major issues since then. Specifically, we shall address the issue of the crack models, where the emphasis will be on smeared formulations. Then, a discussion will follow of some approaches to overcome pathological mesh sensitivity. Finally, three illustrative examples will be given of finite element modelling of crack propagation in plain concrete.

2. On crack modelling

2.1. DISCRETE, SMEARED AND LATTICE-TYPE CRACK MODELLING

Three main approaches exist for modelling cracking in concrete, mortar, masonry and rocks, namely discrete crack models (Ngo and Scordelis, 1967), smeared crack models (Rashid, 1968), while recently the lattice models (van Mier et al., 1994; Schlangen, 1993) have become popular for explaining fracture processes at a detailed level.

In the first method cracking is assumed to occur as soon as the nodal force that is normal to the element boundaries exceeds the maximum tensile force that can be sustained. New degrees-of-freedom at that node location are created and a geometrical discontinuity is assumed to occur between the 'old' node and the newly created node. In the second route of modelling, the cracking process is lumped into the integration points within the elements, where the stress-strain relation is modified to account for the stiffness and strength degradation that accompanies cracking. Finally, in lattice models, originally devised by physicists (Herrmann, et al., 1989; Hrennikoff, 1941), the continuum is replaced *a priori* by lattices of truss or beam elements. Subsequently, the microstructure of the material can be mapped onto these beam elements by assigning them different properties, depending on whether the truss or beam element represents a grain or mortar. For an in-depth discussion the reader is referred to Schlangen and van Mier (van Mier et al., 1994; Schlangen, 1993).

Two main improvements with respect to discrete crack models are the possibilities of remeshing and the use of interface elements as predefined cracks. Remeshing techniques were developed by Ingraffea and his co-workers (Ingraffea and Saouma, 1985; Carter et al., 1995). Using linear-elastic fracture mechanics techniques it is decided where, and in which direction, a crack will propagate. Then, a new mesh is formed in which the crack has propagated over a certain distance. Care must be taken that a proper refinement is applied near the crack tip and that special elements are used which can capture the stress singularity at the crack tip in the linear-elastic solution. A new linear-elastic fracture mechanics analysis is carried out for this geometrically changed structure and on the basis of newly determined stress intensity factors, a new propagation direction is decided upon. Crack extension is assumed in this new direction and a new mesh is set up. The process can then be repeated until complete failure.

While this procedure basically consists of a series of linear-elastic calculations, albeit in an automatised manner, the approach of Rots (1988) to use interface elements as predefined cracks is essentially a fully nonlinear approach. In his procedure interface elements of zero thickness are inserted in the finite element mesh at locations at which a crack is expected to propagate. These locations are chosen either on the basis of smeared-crack analyses or by assessment of experimental data. The interface elements have dual nodes, which have the same coordinates. As in continuum elements the stresses are sampled in integration points between the individual node sets. When the normal stress in an integration remains below the tensile strength the stress-strain relation in the interface is taken as linear elastic, with a high dummy stiffness in order to practically suppress deformations in the interface. When the tensile strength is exceeded in an integration point the unbalanced force thus generated may cause displacements between the two nodes of the node-sets of the interface. We obtain opening (mode-I behaviour) as well as sliding (mode-II behaviour) along the interface element. Of course, the success of this approach crucially depends on a correct estimate of the crack propagation path. Furthermore, the approach is primarily applicable to localised failure where

we indeed have one dominant crack that leads to failure. If these conditions are not fulfilled a discrete-crack analysis along these lines may be less successful.

The success of accurate predictions of the direction of crack propagation in smeared-crack finite element representations depends to a large extent on the tangential shear stiffness of the constitutive relation. A large number of constitutive models have been proposed in the past, which lead to different predictions for the incremental shear stiffness. Sometimes these differences are large, sometimes they are hardly discernible, but they are related to the similarity of some of the fracture formulations.

A possible way to categorise crack models is to divide them into models that are based on a total formulation, i.e. there exists an injective relation between the stresses and the total strains, and models that employ a linear relation between stress rate and strain rate via a loading history dependent on a tangential modulus. Examples of the former category are the elasticity-based fixed crack model, the rotating crack model (Cope et al., 1980), a deformation plasticity theory with a Rankine type yield locus (Feenstra, 1993; Feenstra and de Borst, 1995; Feenstra and de Borst, 1995; Feenstra and de Borst, 1996) and elasticity-based damage models, either isotropic (Mazars, 1984; Mazars and Pijaudier-Cabot, 1989) or anisotropic (Lemaitre and Chaboche, 1990). In the second class of models we have the multidirectional crack model (Rots, 1988; de Borst and Nauta, 1985; de Borst, 1986; de Borst, 1987) and the Rankine model based on a flow theory of plasticity (Feenstra, 1993; Feenstra and de Borst, 1995; Feenstra and de Borst, 1996). Athough major conceptual differences underly the various formulations, remarkable similarities exist especially between plasticity-based models and the familiar rotating crack model when typical nonproportional load paths are simulated. On the other hand the classical fixed crack model gives predictions that significantly differ from most of the other approaches, in the sense that the model response is usually too stiff.

2.2. A CATEGORISATION OF SMEARED-CRACK MODELS

Limiting the discussion to grade-1 materials a total stress-strain relation can be defined as

$$\boldsymbol{\varepsilon} = f(\boldsymbol{\sigma}, \boldsymbol{\eta}, \kappa), \tag{1}$$

with f a tensor-valued function, $\boldsymbol{\varepsilon}$ a strain tensor and $\boldsymbol{\sigma}$ the stress tensor. Equation (1) assumes the existence of a single tensor-valued internal variable, $\boldsymbol{\eta}$, and a single scalar valued internal variable, κ, which reflect the loading history of the material. Extension of this formulation to include more internal variables poses no fundamental problem, but is not necessary for our present purpose. Alternatively, a constitutive formulation can be phrased in rate format, such that

$$\dot{\boldsymbol{\varepsilon}} = f(\boldsymbol{\sigma}, \dot{\boldsymbol{\sigma}}, \boldsymbol{\eta}, \kappa), \tag{2}$$

whereby the dots signify differentiation with respect to a virtual time. A subclass of constitutive models that fits within the framework of (2) are the incrementally-linear models.

$$\dot{\boldsymbol{\varepsilon}} = \mathbf{C}(\boldsymbol{\sigma}, \boldsymbol{\eta}, \kappa)\dot{\boldsymbol{\sigma}}, \tag{3}$$

with $\mathbf{C}$ a tangential compliance tensor.

A simple model that falls into category (1) is elasticity: $\boldsymbol{\varepsilon} = f(\boldsymbol{\sigma})$, which for linear elasticity reduces to $\boldsymbol{\varepsilon} = \mathbf{C}^e\boldsymbol{\sigma}$, with $\mathbf{C}^e$ the fourth-order elastic compliance tensor with the

Young's modulus E and the Poisson's ratio ν as constants for the isotropic case. History dependence can be incorporated in a simple manner by degrading the elastic compliance via a scalar-valued internal parameter ω:

$$\boldsymbol{\varepsilon} = \frac{\mathbf{C}^e \boldsymbol{\sigma}}{1-\omega} \tag{4}$$

or with $\mathbf{D}^e = [\mathbf{C}^e]^{-1}$,

$$\sigma = (1-\omega)\mathbf{D}^e \boldsymbol{\varepsilon}. \tag{5}$$

In this isotropic elasticity-based damage theory the damage variable ω grows from zero to one (complete loss of integrity). Damage growth is possible if the damage loading function

$$f(\varepsilon_{eq}, \kappa) = \varepsilon_{eq} - \kappa \tag{6}$$

vanishes. In (6) ε_{eq} is the equivalent strain, which can be function of the strain invariants, the principal strains as in Mazars (1984)

$$\varepsilon_{eq} = \sqrt{\sum_{i=1}^{3} (\langle \varepsilon_i \rangle)^2}, \tag{7}$$

with ε_i the principal strains, and $\langle \varepsilon_i \rangle = \varepsilon_i$ if $\varepsilon_i > 0$ and $\langle \varepsilon_i \rangle = 0$ otherwise, or the local energy release rate due to damage

$$\varepsilon_{eq} = \tfrac{1}{2} \boldsymbol{\varepsilon}^T \mathbf{C}^e \boldsymbol{\varepsilon}. \tag{8}$$

The parameter κ starts at a damage threshold level κ_0 and is updated by the requirement that during damage growth $f = 0$. In particular, the damage loading function f and the rate of the history parameter κ have to satisfy the discrete Kuhn–Tucker conditions

$$f \leqslant 0, \quad \dot{\kappa} \geqslant 0, \quad f\dot{\kappa} = 0. \tag{9}$$

Damage growth occurs according to an evolution law $F(\kappa)$ such that

$$\omega = F(\kappa). \tag{10}$$

Isotropic damage models have been used successfully in predictions of crack propagation in plain and reinforced concrete (Mazars and Pijaudier-Cabot, 1989). The disadvantage of an isotropic damage model is that possible compressive strut action is eliminated. This disadvantage particularly holds for the analysis of reinforced concrete structures.

Directional dependence of damage evolution can be incorporated by degrading the Young's modulus E in the direction of the major principal stress. When, for planar conditions, distinction is made between the global x, y-coordinate system and a local n, s- coordinate system aligned with the principal stress axes one obtains in the local coordinate system the secant tangential stiffness relation

$$\boldsymbol{\sigma}_{ns} = {}^{s}\mathbf{D}_{ns} \boldsymbol{\varepsilon}_{ns}, \tag{11}$$

with ${}^s\mathbf{D}_{ns}$ defined as

$$ {}^s\mathbf{D}_{ns} = \begin{bmatrix} (1-\omega)E & 0 & 0 \\ 0 & E & 0 \\ 0 & 0 & \beta G \end{bmatrix}, \tag{12} $$

with $\omega = \omega(\varepsilon_{nu})$ and $\beta = \beta(\varepsilon_{nn})$ functions of the normal strain in the local n-direction. The (secant) shear reduction factor β represents the degradation of the elastic stiffness G and is gradually reduced from one to zero. Alternatively, β can be assigned a constant value between zero and one. In a further enhancement Poisson coupling can be added in the secant stiffness relation of the damaged material (Feenstra, 1993).

Let ϕ be the angle between the n and x axes and assume that the directions of principal stress and strain coincide throughout the damage process. Then, the standard transformation rules for second order tensors apply:

$$ \boldsymbol{\varepsilon}_{ns} = \mathbf{T}(\phi)\boldsymbol{\varepsilon}_{xy} \tag{13} $$

and

$$ \boldsymbol{\sigma}_{ns} = \mathbf{T}(\phi)\boldsymbol{\sigma}_{xy}, \tag{14} $$

with $\mathbf{T}$ the standard transformation matrix. Combination of (11), (13) and (14) yields

$$ \boldsymbol{\sigma}_{xy} = \mathbf{T}^T(\phi)\,{}^s\mathbf{D}_{ns}\mathbf{T}(\phi)\boldsymbol{\varepsilon}_{xy}. \tag{15} $$

Equation (15) incorporates the traditional fixed crack model and the rotating crack model. Mathematically, the only difference is that in the fixed crack model the inclination angle ϕ is fixed when the major principal stress first exceeds the tensile strength ($\phi = \phi_0$), while in the rotating crack concept, ϕ changes such that the n-axis continues to coincide with the major principal stress direction. Intuitively, the notion of a fixed crack model is the most appealing: a crack arises perpendicular to the major principal stress direction and once this defect has formed, it remains there. However, considering that in heterogeneous materials like concrete and rock where micro-cracking occurs prior to the formation of a macro-crack, the rotating crack model may be more realistic. Micro-cracks are formed orthogonal to the major principal stress when the tensile strength is first violated. However, upon rotation of the principal stress axes new micro-cracks arise in the 'rotated' direction and it is most likely that upon termination of the stress rotation, the latter micro-cracks will grow into macro-cracks, thus justifying the rotating crack model from a physical perspective.

The above difference has profound consequences when deriving the tangential stiffness, especially with regard to the shear term. For the fixed crack model differentiation of (15) yields

$$ \dot{\boldsymbol{\sigma}}_{xy} = \mathbf{T}^T(\phi_0)\mathbf{D}_{ns}\mathbf{T}(\phi_0)\dot{\boldsymbol{\varepsilon}}_{xy}, \tag{16} $$

with $\mathbf{D}_{ns}$ the local material tangential stiffness matrix:

$$ \mathbf{D}_{ns} = \begin{bmatrix} (1-\omega-\omega'\varepsilon_{nn})E & 0 & 0 \\ 0 & E & 0 \\ \beta'\gamma_{ns}G & 0 & \beta G \end{bmatrix}, \tag{17} $$

where the prime signifies differentiation with respect to ε_{nn}. From (17) we observe that for nonconstant β the local material tangential stiffness matrix becomes nonsymmetric. On the other hand, the requirement of coaxiality between stress and strain tensors that is imposed in the rotating crack model results in a considerably more complicated expression (Rots, 1988; Bažant, 1983; Willam et al., 1986):

$$\dot{\boldsymbol{\sigma}}_{xy} = [\mathbf{T}^T(\phi)\mathbf{D}_{ns}(\mathbf{I}-\mathbf{L})\mathbf{T}(\phi) + \alpha\mathbf{T}^T(\phi)\mathbf{L}\mathbf{T}(\phi)]\dot{\boldsymbol{\varepsilon}}_{xy}, \tag{18}$$

with $\mathbf{I}$ the identity matrix, $\mathbf{L} = \text{diag}[0, 0, -1]$, and $\alpha = (\sigma_{nn}-\sigma_{ss})/[2(\varepsilon_{nn}-\varepsilon_{ss})]$. Comparison of (16) and (18) shows that the *tangential* shear stiffness is now given by α instead of βG. As we shall show in the example to be discussed in the next paragraph α can become negative, leading to a reduction of existing shear stresses and thereby also reducing the existence of locked-in stresses (Rots, 1988).

In all formulations discussed above the strains were recoverable. Upon removal of the load, the strains vanish. This is not so for a deformation type plasticity model, which can also be cast in the format (1). In it the total strain is partitioned into an elastic part $\boldsymbol{\varepsilon}^e$ and an inelastic part $\boldsymbol{\varepsilon}^i$, as follows

$$\boldsymbol{\varepsilon} = \boldsymbol{\varepsilon}^e + \boldsymbol{\varepsilon}^i. \tag{19}$$

The elastic strains are related to the stresses via

$$\boldsymbol{\varepsilon}^e = \mathbf{C}^e\boldsymbol{\sigma}, \tag{20}$$

while the inelastic strains are derivable from a plastic potential f

$$\boldsymbol{\varepsilon}^i = \lambda\frac{\partial f}{\partial \boldsymbol{\sigma}}, \tag{21}$$

where the plastic multiplier λ and $f = f(\boldsymbol{\sigma}, \boldsymbol{\eta}, \kappa)$ must satisfy the discrete Kuhn–Tucker conditions $\lambda \geqslant 0$, $f \leqslant 0$ and $f\lambda = 0$. Accordingly, f also takes the role of a loading function. Combining (19)–(21) results in

$$\boldsymbol{\varepsilon} = \mathbf{C}^e\boldsymbol{\sigma} + \lambda\frac{\partial f}{\partial \boldsymbol{\sigma}}, \tag{22}$$

which, upon elaboration, can be shown to fit the format (1).

We now select the Rankine (major principal stress) criterion as loading function and plastic potential and we introduce the reduced stress tensor $\boldsymbol{\xi} = \boldsymbol{\sigma} - \boldsymbol{\eta}$, with $\boldsymbol{\eta}$ the so-called back stress tensor, which governs the amount of kinematic hardening. In a plane-stress configuration the major principal stress can be expressed in terms of the stress vector with the aid of Mohr's circle and one obtains

$$f = \sqrt{\tfrac{1}{2}\boldsymbol{\xi}^T\mathbf{P}\boldsymbol{\xi}} + \tfrac{1}{2}\boldsymbol{\pi}^T\boldsymbol{\xi} - \bar{\sigma}(\gamma\kappa) \tag{23}$$

with the equivalent stress $\bar{\sigma}$ a function of the internal parameter κ, and γ a factor which sets the ratio between kinematic hardening/softening and isotropic hardening/softening. Pure kinematic hardening is obtained for $\gamma = 0$ and $\gamma = 1$ sets the other limiting case of pure

isotropic hardening/softening. The projection matrix $\mathbf{P}$ and the projection vector $\boldsymbol{\pi}$ are given by

$$\mathbf{P} = \begin{bmatrix} \frac{1}{2} & -\frac{1}{2} & 0 \\ -\frac{1}{2} & \frac{1}{2} & 0 \\ 0 & 0 & 2 \end{bmatrix} \tag{24}$$

and

$$\boldsymbol{\pi} = [1, 1, 0]^T \tag{25}$$

respectively. The equivalent stress $\bar{\sigma}(\gamma\kappa)$ is the current uniaxial tensile strength which starts at the initial tensile strength f_t and is gradually reduced according to some tension-softening model. The internal parameter κ is assumed to be a measure for the internal damage and is supposed to be determined by a work-hardening hypothesis

$$\kappa\bar{\sigma} = \boldsymbol{\xi}^T\boldsymbol{\varepsilon}^i. \tag{26}$$

The back stress $\boldsymbol{\eta}$ is given by

$$\boldsymbol{\eta} = \lambda(1-\gamma)E_{ks}\boldsymbol{\Lambda}\frac{\partial f}{\partial \boldsymbol{\sigma}}, \tag{27}$$

with E_{ks} a secant stiffness modulus and $\boldsymbol{\Lambda} = \text{diag}[1, 1, \frac{1}{2}]$. A rationale for this formulation has been given by Feenstra (1993).

Alternatively, the Rankine yield criterion (23) can be used within the framework of a flow theory of plasticity. While the strain decomposition (19) and the relation for the elastic strains (20) remain unaffected, a direct expression for the inelastic strain in the sense of (21) is no longer assumed. Instead, an expression for the inelastic strain *rate* is adopted

$$\dot{\boldsymbol{\varepsilon}}^i = \dot{\lambda}\frac{\partial f}{\partial \boldsymbol{\sigma}}, \tag{28}$$

where the plastic flow rate $\dot{\lambda}$ must satisfy the Kuhn–Tucker conditions: $\dot{\lambda} \geqslant 0, f \leqslant 0$ and $f\dot{\lambda} = 0$. In a similar spirit we now have to define evolution equations for the rate of the internal hardening/softening parameter κ

$$\dot{\kappa}\bar{\sigma} = \boldsymbol{\xi}^T\dot{\boldsymbol{\varepsilon}}^i, \tag{29}$$

and the back stress rate

$$\dot{\boldsymbol{\eta}} = \dot{\lambda}(1-\gamma)E_{ks}\boldsymbol{\Lambda}\frac{\partial f}{\partial \boldsymbol{\sigma}}. \tag{30}$$

It is noted that differentiation of (19)–(20) and combination with (28) results in

$$\dot{\boldsymbol{\varepsilon}} = \mathbf{C}^e\dot{\boldsymbol{\sigma}} + \dot{\lambda}\frac{\partial f}{\partial \boldsymbol{\sigma}}, \tag{31}$$

which, upon further elaboration can be shown to fall within the format (3).

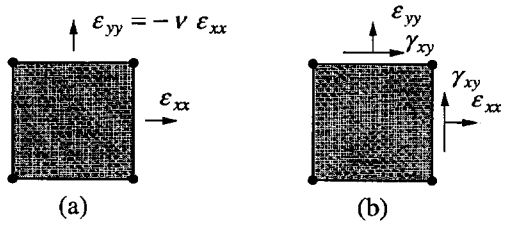

Figure 1. Tension–shear model problem: (a) tension up to cracking; (b) biaxial tension with shear beyond cracking.

2.3. AN ELEMENTARY TENSION-SHEAR MODEL PROBLEM

The fundamental differences of the formulations discussed so far will be elucidated with an elementary problem proposed by Willam et al. (1986), in which a plane-stress element with unit dimensions is loaded in biaxial tension and shear. This causes a continuous rotation of the principal strain axes after cracking, as is typical of crack propagation in smeared crack finite element analysis. The element is subjected to tensile straining in the x-direction accompanied by lateral Poisson contraction in the y-direction to simulate uniaxial loading. Immediately after the tensile strength has been violated, the element is loaded in combined biaxial tension and shear strain (Figure 1). The ratio between the different strain components is given by $\Delta\varepsilon_{xx}:\Delta\varepsilon_{yy}:\Delta\gamma_{xy} = 0.5:0.75:1$. The reference set of material parameters is: Young's modulus $E = 10,000\,\text{MPa}$, Poisson's ratio $\nu = 0.2$, tensile strength $f_t = 1.0\,\text{MPa}$. A linear strain softening diagram with a fracture energy $G_f = 0.15 \times 10^{-3}\,\text{N/mm}$ has been used. (An in-depth discussion of the role of the fracture energy parameter G_f in analyses of crack propagation will be presented in the next section).

The behaviour of the different formulations for smeared cracking can be studied in detail with this problem. The constitutive behaviour will be compared with respect to the shear stress–shear strain behaviour and the normal stress–normal strain behaviour in the x and y-directions. Particularly the shear stress–shear strain response gives a good impression of the behaviour of the model when applied to the analyses of structures. The first issue which will be treated is the different behaviour of the models formulated in the total strain concept. The comparison between the isotropic damage model, the rotating crack model and the Rankine deformation plasticity model with isotropic and kinematic hardening should make clear which models are capable of predicting a flexible shear stress–shear strain response. The second issue is the comparison of the rotating crack model and the Rankine plasticity model within an incremental format. Because the response of models with a total formulation is in general more flexible than the response of models with an incremental formulation, we expect that the Rankine plasticity model with an incremental formulation will show a less flexible shear stress–shear strain response, but the comparison should provide insight if this less flexible response is still acceptable.

The shear stress–shear strain response of the fixed and rotating crack models and the deformation theory based plasticity models is shown in Figure 2. The fixed crack model has been used with a shear reduction factor $\beta = 0.05$, which results in a monotonically increasing shear stress with increasing shear strain, Figure 2. The rotating crack model shows an implicit shear softening behaviour which has been observed previously (Rots, 1988, Willam et al., 1986). It is interesting that the same behaviour occurs for the deformation plasticity model either with isotropic or with kinematic hardening. The two formulations are in fact

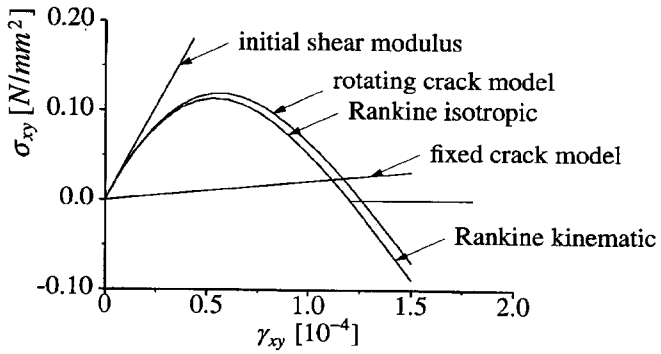

Figure 2. Total formulation of the constitutive models. $\sigma_{xy} - \gamma_{xy}$ response.

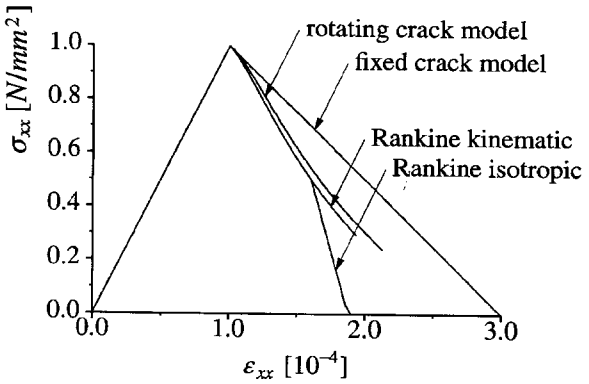

Figure 3. Total formulation of the constitutive models. $\sigma_{xx} - \varepsilon_{xx}$ response.

indiscernible until the shear stress has almost softened completely. Then the isotropic and the kinematic hardening models yield different responses which are due to the fact that with isotropic hardening it is impossible for the shear stress to become negative for positive increments of the shear strain component of the strain vector. It is obvious from Figure 2 that the differences between the various models are small. Only the fixed crack model gives a completely different response.

The $\sigma_{xx} - \varepsilon_{xx}$ response depicted in Figure 3 shows that the input stress–strain softening diagram is exactly reproduced by the fixed crack model. This is logical, since the softening has been monitored in the fixed crack directions which are aligned with the $x - y$-axes. The behaviour of the other models shows an implicit normal stress-shear stress coupling. The Rankine plasticity model with isotropic softening shows a progressive degradation of the stiffness until the stress has been decreased to approximately 50 percent which is attended with a zero shear stress. At this stage the apex of the yield surface has been reached and the stress components in x and y-direction are softening in the direction of the origin. The response in the lateral y-direction is shown in Figure 4 which shows the formation of a secondary crack perpendicular to the first crack for the fixed crack model which again reflects the input softening diagram. The rotating crack model and the Rankine plasticity model with kinematic softening show a gradual degradation of the stiffness in the y-direction (Figure 4). This can also be observed for the Rankine plasticity model with isotropic softening until the shear stress

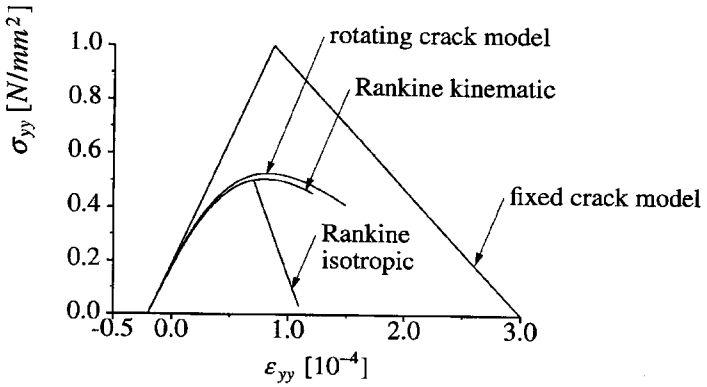

Figure 4. Total formulation of the constitutive models. $\sigma_{yy} - \varepsilon_{yy}$ response.

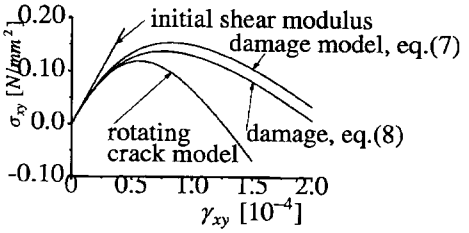

Figure 5. Damage models and the rotating crack model. $\sigma_{xy} - \gamma_{xy}$ response.

becomes equal to zero and the stress in the y-direction begins to soften linearly which is in accordance with the input softening diagram.

Although the tendencies are the same, somewhat larger differences exist between the rotating crack model and the deformation-type plasticity theories on one hand and, on the other hand, the isotropic damage models as formulated in (5)–(10). In particular the shear stress response is stiffer, although to a lesser extent for the equivalent strain definition via the local energy release rate (8) than for that of Mazars (7), Figure 5. While the $\sigma_{xx} - \varepsilon_{xx}$ curves are rather similar, Figure 6, the $\sigma_{yy} - \varepsilon_{yy}$ responses displayed in Figure 7 show that the isotropic damage models react much softer. This observation is an inherent property of the isotropic character of the damage model.

The performance of the constitutive models based on a total formulation has been shown with the elementary tension-shear model problem. The formulation of a maximum principal stress criterion within the framework of elasticity or within the framework of plasticity does not result in major differences. In particular, the elasticity-based rotating crack model and the Rankine plasticity model with kinematic hardening show an almost identical behaviour. The behaviour of the Rankine model with isotropic hardening is identical to the behaviour of the Rankine model with kinematic hardening until the shear stress is equal to zero. At that stage the apex of the yield surface has been reached for the isotropic hardening model and the shear stress is equal to zero.

The limiting case with no softening ($G_f = \infty$) confirms that the different formulations within the total strain concept result in a similar behaviour. The shear stress-shear strain responses of the rotating crack model and the Rankine plasticity model are shown in Figure 8.

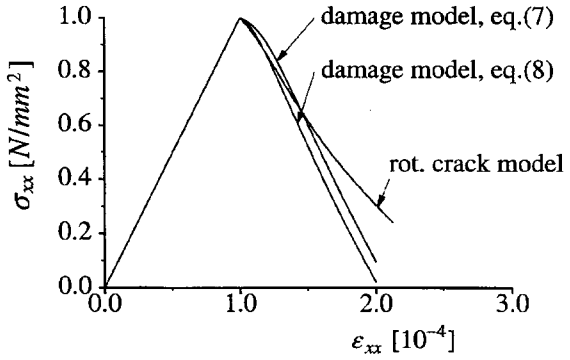

Figure 6. Damage models and the rotating crack model. $\sigma_{xx} - \varepsilon_{xx}$ response.

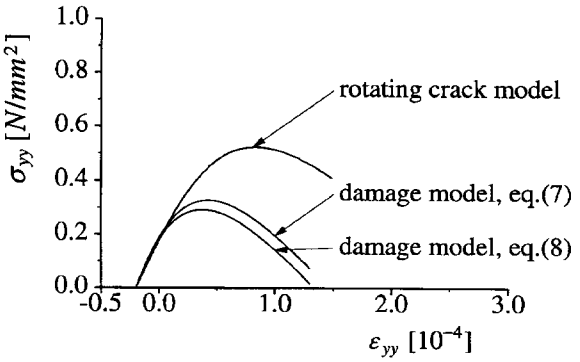

Figure 7. Damage models and the rotating crack model. $\sigma_{yy} - \varepsilon_{yy}$ response.

The response is identical for all models with a total formulation. It is clear from this figure that although no softening has been assumed, the shear stress-shear strain response shows an implicit softening behaviour. Figure 8 also shows the response of the Rankine model formulated within an incremental concept, which displays a shear stress–shear strain response that is less flexible, but still results in an implicit shear softening. The coincidence between the rotating crack model and the Rankine plasticity model based on the deformation theory for ideal plasticity has also been shown in Crisfield and Wills (1989).

The plasticity model based on an incremental formulation has also been applied to the tension–shear model problem with the standard softening material properties and compared with the rotating crack model in the following figures. The major interest concerns the behaviour in shear which is depicted in Figure 9. It is clear that the rotating crack model has the most flexible response in shear, but the differences between the rotating crack model and the plasticity model are minor. Again, the Rankine plasticity model with isotropic hardening results in a shear stress equal to zero when the apex of the yield surface has been reached.

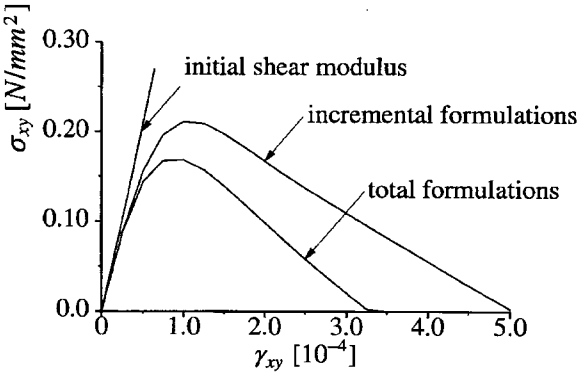

Figure 8. $G_f = \infty$. $\sigma_{xy} - \gamma_{xy}$ response.

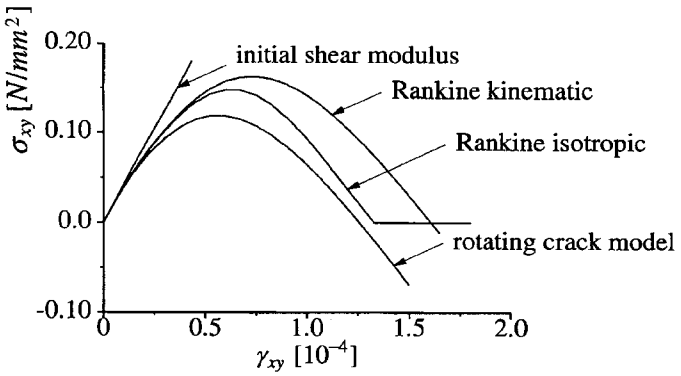

Figure 9. Tangential formulations and the rotating crack model. $\sigma_{xy} - \gamma_{xy}$ response.

3. Cracking, damage and localisation of deformation

3.1. Fundamental causes and implications for numerical models

A major problem when using a standard, rate-independent continuum for modelling degradation processes such as smeared cracking is that beyond a certain level of damage accumulation the governing set of partial differential equations locally changes type. In the static case the elliptic character of the set of partial differential equations is lost, while, on the other hand, in the dynamic case we observe a change of a hyperbolic set into an elliptic set. In both cases the rate boundary value problem becomes ill-posed and numerical solutions suffer from pathological mesh sensitivity.

The inadequacy of the standard, rate-independent continuum to model failure zones correctly is due to the fact that *force-displacement relations* measured in testing devices are simply mapped onto *stress-strain curves* by dividing the force and the elongation by the original load-carrying area and the original length of the specimen, respectively. This is done without taking into account the changes in the micro-structure that occur when the material is so heavily damaged as in fracture processes. Therefore, the mathematical description ceases to be a meaningful representation of the physical reality.

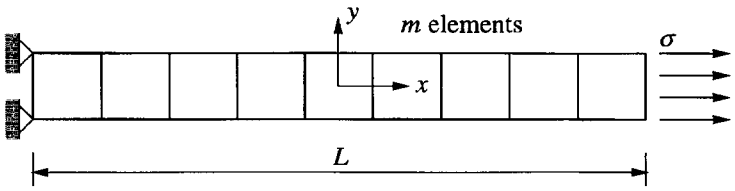

Figure 10. Strain-softening bar subject to uniaxial loading.

To solve this problem one must either introduce additional terms in the continuum description which reflect the changes in the micro-structure that occur during fracture, or one must take into account the viscosity of the material. In both cases the effect is that the governing equations do not change type during the damage evolution process and that physically meaningful solutions are obtained for the entire loading range (regularisation procedures). It is emphasised that although concrete can be regarded as a disordered material, the introduction of stochastic distributions of defects does not replace the need for the introduction of regularisation procedures (Carmeliet and de Borst, 1995). For a proper description of failure in concrete both enhancements are necessary: enrichment of the continuum by higher-order terms, either in space or in time, and the introduction of the occurrence of material flaws as a stochastic quantity.

Another way to look upon the introduction of additional terms in the continuum description is that the Dirac distributions for the strain at failure are replaced by continuous strain distributions, which lend themselves for description by standard numerical schemes. Although the strain gradients are now finite, they may be very steep and the concentration of strain in a small area can still be referred to as *strain localisation or localisation of deformation.*

The essential deficiency of the standard continuum model can be demonstrated simply by the example of a simple bar loaded in uniaxial tension, Figure 10 (Crisfield, 1982; de Borst, 1987). Let the bar be divided into m elements. Prior to reaching the tensile strength f_t, a linear relation is assumed between the (normal) stress σ and the (normal) strain $\varepsilon, \sigma = E\varepsilon$, with E Young's modulus. After reaching the peak strength a descending slope is defined in this diagram through an affine transformation from the measured load-displacement curve. The result is given in the left part of Figure 11, where ε_u marks the point where the load-carrying capacity is totally exhausted. In the post-peak regime the constitutive model can thus be written as:

$$\sigma = f_t + h(\varepsilon - \varepsilon_0). \tag{32}$$

In case of degrading materials $h < 0$ and h may be termed a softening modulus.

Now suppose that one element has a tensile strength that is marginally below that of the other $m - 1$ elements. Upon reaching the tensile strength of this element failure will occur. In the other neighbouring elements the tensile strength is not exceeded and they will unload elastically. The result on the *average* strain of the bar $\bar{\varepsilon}$ is plotted in the right part of Figure 11 for different discretisations of the bar. The results are fully dominated by the discretisation, and convergence to a 'true' post-peak failure curve does not seem to occur. In fact, it does occur, as the failure mechanism in a standard continuum is a line crack with zero thickness. The finite element solution of our continuum rate boundary value problem simply tries to capture this line crack, which results in localisation in one element, irrespective of the

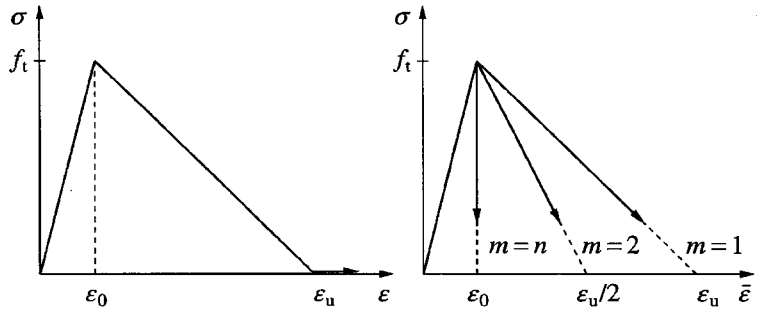

Figure 11. Stress-strain diagram (left) and response of an imperfect bar in terms of a stress-average strain curve (right).

width of this element. The result on the load-average strain curve is obvious: for an infinite number of elements ($m \to \infty$) the post-peak curve doubles back on the original loading curve. Numerous numerical examples for all sorts of materials exist which further illustrate the above argument. From a physical point of view this is unacceptable and we must therefore either rephrase our constitutive model in terms of force-displacement relations, which implies the use of special interface elements (Rots, 1988; Schellekens, 1992) or enriching the continuum description by adding higher-order terms which can accommodate narrow zones of highly localised deformation quite similar to descriptions for boundary layers in fluids.

3.2. CRACK BAND MODELS

As an intermediate solution between using the standard continuum model and adding higher-order terms the Crack Band Model has been proposed (Bažant and Oh, 1983), in which the area under the softening curve in the left part of Figure 11 is considered as a material parameter, the so-called fracture energy:

$$G_f = \int \sigma \, \mathrm{d}u = \int \sigma \varepsilon(s) \, \mathrm{d}s. \tag{33}$$

When we prescribe the fracture energy G_f as an additional material parameter the global load-displacement response can become insensitive to the discretisation. In finite element calculations the crack localises in a band that is one or a few elements wide, depending on the element type, the element size, the element shape and the integration scheme. In Feenstra (1993) it is assumed that the width over which the fracture energy is distributed can be related to the area of an element

$$h = \alpha_h \sqrt{A_e} = \alpha_h \left(\sum_{\xi=1}^{n_\xi} \sum_{\eta=1}^{n_\eta} \det(\mathbf{J}) w_\xi w_\eta \right)^{\frac{1}{2}} \tag{34}$$

in which w_ξ and w_η are the weight factors of the Gaussian integration rule as it is tacitly assumed that the elements are integrated numerically. The local, isoparametric coordinates of the integration points are given by ξ and η, and $\det(\mathbf{J})$ is the Jacobian of the transformation between the local, isoparametric coordinates and the global coordinate system. The factor α_h

is a modification factor which is equal to one for quadratic elements and equal to $\sqrt{2}$ for linear elements (Rots, 1988).

Although the introduction of a fracture energy is a major improvement in calculations using any smeared-crack concept, locally nothing has altered and localisation continues to take place in one row of elements (or better: one row of integration points). This is logical, since the loss of ellipticity still occurs locally, even though the energy that is dissipated remains constant by adapting the softening modulus to the element size. For numerical simulations this implies for instance that severe convergence problems are usually encountered if the mesh is refined or if in addition to matrix failure the possibility of interface debonding between matrix and grains is modelled by inserting interface elements in the numerical model (Schellekens, 1992). Also, the frequently reported observation still holds that the localisation zones are biased by the discretisation and tend to propagate along the mesh lines. This has been demonstrated nicely by the example of impact loading on a concrete specimen in a Split–Hopkinson device (Sluys, 1992; Sluys and de Borst, 1996).

The deficiency of the standard continuum model with regard to properly describing strain localisation can be overcome by introducing higher-order terms in the continuum description, which are thought to reflect the microstructural changes that take place at a level below the continuum level. Examples of such changes are void formation in metals and crack bridging phenomena in the context of concrete (van Mier, 1991). Essentially, one then departs from the concept of a 'simple' solid which has been the starting point for virtually all modern developments in continuum mechanics. A number of suggestions have been put forward for non-standard continuum descriptions that are capable of properly incorporating failure zones, see the Introduction for an overview. Herein we shall limit ourselves to non-local and gradient damage models.

3.3. NON-LOCAL DAMAGE MODELS

In a non-local generalisation the equivalent strain ε_{eq} is normally replaced by a spatially averaged quantity (Pijaudier-Cabot and Bažant, 1987):

$$f(\bar{\varepsilon}_{eq}, \kappa) = \bar{\varepsilon}_{eq} - \kappa, \tag{35}$$

where the non-local average strain $\bar{\varepsilon}_{eq}$ is computed as:

$$\bar{\varepsilon}_{eq}(\mathbf{x}) = \frac{1}{V_r(\mathbf{x})} \int_V g(\mathbf{s}) \varepsilon_{eq}(\mathbf{x}+\mathbf{s})\, \mathrm{d}V, \quad V_r(\mathbf{x}) = \int_V g(\mathbf{s})\, \mathrm{d}V, \tag{36}$$

with $g(\mathbf{s})$ a weight function, e.g., the error function, and $\mathbf{s}$ a relative position vector pointing to the infinitesimal volume $\mathrm{d}V$. Alternatively, the locally defined history parameter κ may be replaced in the damage loading function f by a spatially averaged quantity:

$$f(\varepsilon_{eq}, \bar{\kappa}) = \varepsilon_{eq} - \bar{\kappa}, \tag{37}$$

where the non-local history parameter $\bar{\kappa}$ follows from:

$$\bar{\kappa}(\mathbf{x}) = \frac{1}{V_r(\mathbf{x})} \int_V g(\mathbf{s}) \kappa(\mathbf{x}+\mathbf{s})\, \mathrm{d}V, \quad V_r(\mathbf{x}) = \int_V g(\mathbf{s})\, \mathrm{d}V. \tag{38}$$

The Kuhn–Tucker conditions can now be written as:

$$f \leqslant 0, \quad \dot{\kappa} \geqslant 0, \quad f\dot{\kappa} = 0. \tag{39}$$

3.4. GRADIENT DAMAGE MODELS

Non-local constitutive relations can be considered as a point of departure for constructing gradient models. Again, this can either be done by expanding the kernel ε_{eq} of the integral in (36) in a Taylor series, or by expanding the history parameter κ in (38) in a Taylor series. First, we will expand ε_{eq} and then we will do the same for κ. If we truncate after the second-order terms and carry out the integration implied in (36) under the assumption of isotropy, the following relation ensues:

$$\bar{\varepsilon}_{eq} = \varepsilon_{eq} + \bar{c}\nabla^2\varepsilon_{eq}, \tag{40}$$

where $\bar{c}$ is a material parameter of the dimension length squared. It can be related to the averaging volume and then becomes dependent on the precise form of the weight function g. For instance, for a one-dimensional continuum and taking

$$g(s) = \frac{1}{\sqrt{2\pi}l}\, \mathrm{e}^{-s^2/2l^2}, \tag{41}$$

we obtain $\bar{c} = \frac{1}{2}l^2$. Here, we adopt the phenomenological view that $\sqrt{\bar{c}}$ reflects the length scale of the failure process that we wish to describe macroscopically.

Formulation (40) has a severe disadvantage when applied in a finite element context, namely that it requires computation of second-order gradients of the local equivalent strain ε_{eq}. Since this quantity is a function of the strain tensor, and since the strain tensor involves first-order derivatives of the displacements, third-order derivatives of the displacements have to be computed, which necessitates C^1- continuity of the shape functions. To obviate this problem, (40) is differentiated twice and the result is substituted in (40). Again neglecting fourth-order terms then leads to

$$\bar{\varepsilon}_{eq} - \bar{c}\nabla^2\bar{\varepsilon}_{eq} = \varepsilon_{eq}. \tag{42}$$

When $\bar{\varepsilon}_{eq}$ is discretised independently and use is made of the divergence theorem, a C^0-interpolation for $\bar{\varepsilon}_{eq}$ suffices (Peerlings et al., 1996).

Higher-order continua require additional boundary conditions. With (42) governing the damage process, either the averaged equivalent strain $\bar{\varepsilon}_{eq}$ itself or its normal derivative must be specified on the boundary S of the body:

$$\bar{\varepsilon}_{eq} = \bar{\varepsilon}_s \quad \text{or} \quad \mathbf{n}^T\nabla\bar{\varepsilon} = \bar{\varepsilon}_{ns}, \tag{43}$$

with $\mathbf{n}$ the outward normal vector to the boundary of the body S. In most calculations the natural boundary condition $\bar{\varepsilon}_{ns} = 0$ is adopted.

In a fashion similar to the derivation of the gradient damage models based on the averaging of the equivalent strain ε_{eq}, we can elaborate a gradient approximation of (38), i.e., by

developing κ into a Taylor series. For an isotropic, infinite medium and truncating after the second term we then have

$$\bar{\kappa} = \kappa + \bar{c}\nabla^2\kappa, \tag{44}$$

where the gradient constant $\bar{c}$ again depends on the weighting function. In principle (37) could now be replaced by

$$f = \varepsilon_{eq} - \kappa - \bar{c}\nabla^2\kappa, \tag{45}$$

but we will consider κ as an independent variable in the finite element implementation to be discussed next, and therefore we shall retain the form (37) for the damage loading function, where $\bar{\kappa}$ is given by (44).

3.5. FINITE ELEMENT ASPECTS

As an example we shall elaborate the finite element implementation of the damage model with gradient enhancement according to (44). We consider equilibrium at iteration $n+1$:

$$\mathbf{L}^T\boldsymbol{\sigma}_{n+1} + \rho\mathbf{g} = \mathbf{0}, \tag{46}$$

with $\mathbf{g}$ the gravity acceleration vector and $\mathbf{L}$ a differential operator matrix. Multiplying the equilibrium equation with $\delta\mathbf{u}$, where $\mathbf{u}$ is the continuous displacement field vector and the symbol δ denotes the variation of a quantity, and integrating over the entire volume occupied by the body, one obtains the corresponding weak form:

$$\int_V \delta\mathbf{u}^T(\mathbf{L}^T\boldsymbol{\sigma}_{n+1} + \rho\mathbf{g})\,\mathrm{d}V = 0. \tag{47}$$

Similarly, the weak form of the Helmholtz equation for the distribution of the local history parameter κ, (44), can be derived as:

$$\int_V \delta\kappa(\kappa_{n+1} + \bar{c}\nabla^2\kappa_{n+1} - \bar{\kappa}_{n+1})\,\mathrm{d}V = 0. \tag{48}$$

We now introduce the decompositions

$$\boldsymbol{\sigma}_{n+1} = \boldsymbol{\sigma}_n + d\boldsymbol{\sigma} \tag{49}$$

and

$$\kappa_{n+1} = \kappa_n + d\kappa \tag{50}$$

for the stress $\boldsymbol{\sigma}$ and the history parameter κ, respectively. The d-symbol signifies the iterative improvement of a quantity between two successive iterations. With aid of these decompositions and applying the divergence theorem to (47)–(48) one obtains

$$\int_V (\mathbf{L}\delta\mathbf{u})^T\,\mathrm{d}\boldsymbol{\sigma}\,\mathrm{d}V = \int_V \rho\delta\mathbf{u}^T\mathbf{g}\,\mathrm{d}V + \int_S \delta\mathbf{u}^T\mathbf{t}\,\mathrm{d}S - \int_V (\mathbf{L}\delta\mathbf{u})^T\boldsymbol{\sigma}_n\,\mathrm{d}V, \tag{51}$$

where $\mathbf{t}$ is the boundary-traction vector and

$$\int_V (\delta\kappa \, \mathrm{d}\kappa - \bar{c}\nabla\delta\kappa \cdot \nabla \, \mathrm{d}\kappa) \, \mathrm{d}V - \int_V \delta\kappa \, \mathrm{d}\bar{\kappa} \, \mathrm{d}V$$
$$= \int_V \delta\kappa\bar{\kappa}_n \, \mathrm{d}V - \int_V (\delta\kappa\kappa_n - \bar{c}\nabla\delta\kappa \cdot \nabla\kappa_n) \, \mathrm{d}V, \tag{52}$$

where the non-standard natural boundary condition

$$\mathbf{n}^T\nabla\kappa = 0 \tag{53}$$

has been adopted, $\mathbf{n}$ being the outward normal to the body surface. Since κ can be directly related to the damage variable ω this condition can be interpreted as no damage flux through the boundary of the body, which seems physically reasonable.

Finally we interpolate displacements $\mathbf{u}$ and the history parameter κ as

$$\mathbf{u} = \mathbf{H}\mathbf{a} \quad \text{and} \quad \kappa = \tilde{\mathbf{H}}\mathbf{k}, \tag{54}$$

with $\mathbf{a}$ and $\mathbf{k}$ the vectors that contain the nodal values of $\mathbf{u}$ and κ, respectively. $\mathbf{H}$ and $\tilde{\mathbf{H}}$ contain the interpolation polynomials of $\mathbf{u}$ and κ, respectively. The gradient of κ is then computed as

$$\nabla\kappa = \tilde{\mathbf{B}}\mathbf{k}, \quad \tilde{\mathbf{B}} = \nabla \cdot \tilde{\mathbf{H}} \tag{55}$$

and, restricting the treatment to small deformation gradients, we obtain for the strain tensor:

$$\boldsymbol{\varepsilon} = \mathbf{B}\mathbf{a}, \quad \mathbf{B} = \mathbf{L}\mathbf{H}. \tag{56}$$

Substitution of (54)–(55) into (51) and (52), casting the standard elastic-damage stress-strain relation of (5) into an incremental format, and using the fact that the ensuing relations must hold for any admissible $\delta\mathbf{u}$ and $\delta\kappa$ finally yields the following set of equations that describe the incremental process in the discretised gradient-enhanced elastic-damaging continuum (de Borst et al, 1997):

$$\begin{bmatrix} \mathbf{K}_{aa} & \mathbf{K}_{ak} \\ \mathbf{K}_{ka} & \mathbf{K}_{kk} \end{bmatrix} \begin{bmatrix} \mathrm{d}\mathbf{a} \\ \mathrm{d}\mathbf{k} \end{bmatrix} = \begin{bmatrix} \mathbf{f}_{ext} - \mathbf{f}_{int,n} \\ \mathbf{f}_{k,n} - \mathbf{K}_{kk}\mathbf{k}_n \end{bmatrix} \tag{57}$$

where

$$\mathbf{K}_{aa} = \int_V (1 - \omega_n)\mathbf{B}^T\mathbf{D}^e\mathbf{B} \, \mathrm{d}V, \tag{58}$$

$$\mathbf{K}_{ak} = \int_V \mathbf{B}^T\mathbf{D}^e\boldsymbol{\varepsilon}_n \frac{\partial\omega}{\partial\kappa}\tilde{\mathbf{H}} \, \mathrm{d}V, \tag{59}$$

$$\mathbf{K}_{ka} = \int_V \frac{\partial\bar{\kappa}}{\partial\varepsilon_{eq}}\tilde{\mathbf{H}}^T\frac{\partial\varepsilon_{eq}}{\partial\boldsymbol{\varepsilon}}\mathbf{B} \, \mathrm{d}V, \tag{60}$$

$$\mathbf{K}_{kk} = \int_V (\tilde{\mathbf{H}}^T\tilde{\mathbf{H}} - \bar{c}\tilde{\mathbf{B}}^T\tilde{\mathbf{B}}) \, \mathrm{d}V \tag{61}$$

and

$$\mathbf{f}_{ext} = \int_V \rho \mathbf{H}^T \mathbf{g} \, \mathrm{d}V + \int_S \mathbf{H}^T \mathbf{t} \, \mathrm{d}S, \tag{62}$$

$$\mathbf{f}_{int,n} = \int_V \mathbf{B}^T \boldsymbol{\sigma}_n \, \mathrm{d}V, \tag{63}$$

$$\mathbf{f}_{k,n} = \int_V \tilde{\mathbf{H}}^T \bar{\kappa}_n \, \mathrm{d}V. \tag{64}$$

An algorithm is elaborated in Box 1.

Box 1. Algorithm for gradient-enhanced damage model.

1. Update $\mathbf{K}_{aa}, \mathbf{K}_{ak}, \mathbf{K}_{ka}$
2. Solve for $\mathrm{d}\mathbf{a}$ and $\mathrm{d}\mathbf{k}$ using (57)
3. Update $\mathbf{a}$ and $\mathbf{k}$ at the nodal points:

   $\mathbf{a}_{n+1} = \mathbf{a}_n + \mathrm{d}\mathbf{a}$
   $\mathbf{k}_{n+1} = \mathbf{k}_n + \mathrm{d}\mathbf{k}$
4. Compute in the integration points:

   strains: $\boldsymbol{\varepsilon}_{n+1} = \mathbf{B}\mathbf{a}_{n+1}$
   equivalent strain: $\varepsilon_{eq,n+1} = \varepsilon_{eq}(\boldsymbol{\varepsilon}_{n+1})$
   damage loading function: $f = \varepsilon_{eq,n+1} - \bar{\kappa}_n$
   If $f \geqslant 0$: $\bar{\kappa}_{n+1} = \varepsilon_{eq,n+1}$
   else: $\bar{\kappa}_{n+1} = \bar{\kappa}_n$
   Interpolate: $\kappa_{n+1} = \tilde{\mathbf{H}}\mathbf{k}_{n+1}$
   Compute: $\omega_{n+1} = \omega(\kappa_{n+1})$
   Compute: $\boldsymbol{\sigma}_{n+1} = (1 - \omega_{n+1})\mathbf{D}\boldsymbol{\varepsilon}_{n+1}$
5. Update the internal forces:

   $$\mathbf{f}_{int,n+1} = \int_V \mathbf{B}^T \boldsymbol{\sigma}_{n+1} \, \mathrm{d}V$$

   $$\mathbf{f}_{k,n+1} = \int_V \tilde{\mathbf{H}}^T \bar{\kappa}_{n+1} \, \mathrm{d}V$$
6. Check convergence criterion.

Because the basic variables are differentiated only once in the above expressions, a simple C^0-continuity of the interpolation polynomials suffices. To avoid stress oscillations, the displacements should be interpolated one order higher than the history variable, cf. the Babuška–Brezzi condition for mixed finite elements in incompressible solids.

4. Applications to fracture in plain concrete

4.1. A SPLITTING TEST

For planar structures in which tension-compression or compression-compression stress states play an important role the major principal stress criterion for crack initiation must be augmented by a separate yield locus, which bounds the stress states in the tension-compression and the compression-compression regime. It has been shown by Feenstra (1993) that the experiments of Kupfer and Gerstle (1973) for plain concrete subjected to proportional biaxial loading, can be used to define a composite failure surface with a Von Mises type yield contour in the compression-compression regime and a Rankine (major principal stress) failure condition in the tensile regime. Neglecting possible kinematic softening effects ($\gamma = 1$), this composite yield function is then given by

$$\begin{cases} f_c = \sqrt{\frac{1}{2}\boldsymbol{\sigma}^T \mathbf{Q} \boldsymbol{\sigma}} & -\bar{\sigma}_c(\kappa_c) \\ f_t = \sqrt{\frac{1}{2}\boldsymbol{\sigma}^T \mathbf{P} \boldsymbol{\sigma}} + \frac{1}{2}\boldsymbol{\pi}^T \boldsymbol{\sigma} & -\bar{\sigma}_t(\kappa_t) \end{cases}, \tag{65}$$

with

$$\mathbf{Q} = \begin{bmatrix} 2 & -1 & 0 \\ -1 & 2 & 0 \\ 0 & 0 & 6 \end{bmatrix}. \tag{66}$$

The constitutive behaviour is now completely governed by the equivalent stresses, $\bar{\sigma}_c(\kappa_c)$ and $\bar{\sigma}_t(\kappa_t)$ as nonlinear functions of the internal parameters κ_c and κ_t, respectively (Feenstra, 1993). The fit between the experimental data and the composite plasticity model defined in (66) is shown in Figure 12.

The uniaxial compressive stress-strain curve can be approximated by different functions (Vecchio and Collins, 1982; CEB-FIP, 1990). However, these relations are not energy-based formulations, and the results will therefore significantly depend on the finite element discretisation. Following Feenstra (1993), the behaviour in compression will be modelled with a compression softening model in which, similar to the Crack Band Model for tensile loadings, a compressive fracture energy is introduced, G_c. The quintessence of the compression-equivalent of the Crack Band Model is that the maximum equivalent strain in compression κ_{uc} is related to the compression fracture energy G_c and to the element size h. Experimental evidence for the assumption that the compressive fracture energy G_c can be considered as a material parameter has been provided by Vonk (1992).

The application concerns a splitting test which is often used as an indirect test for determining the tensile strength of concrete (Feenstra, 1993). This example has been chosen to analyse the capability of a composite plasticity model to predict the failure mode in a tension-compression test. The specimen which will be analysed is a cube with a side of 150 mm. Only a half of the specimen has been discretised because of symmetry conditions, with two different discretisations in order to show mesh-insensitivity. The two meshes are shown in Figure 13. The first discretisation consists of 21 × 9 cross-diagonal constant strain triangles with a total number of elements equal to 756. The second discretisation concerns a refinement with a factor nine, resulting in a total number of elements equal to 6804. The loading

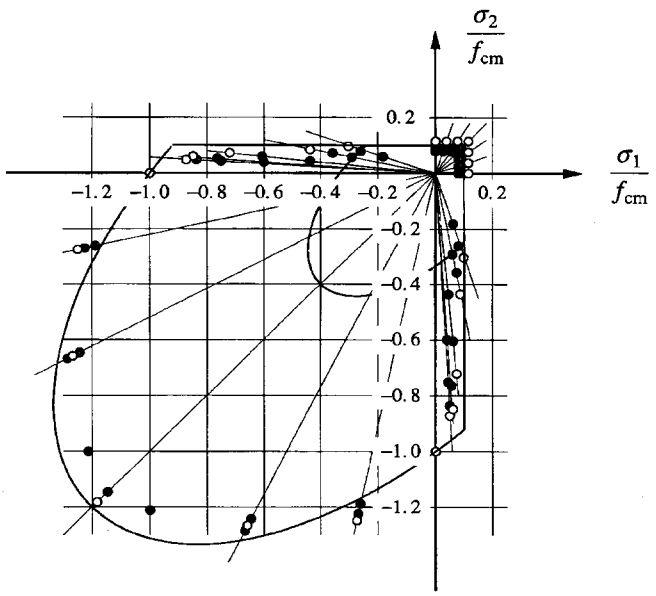

Figure 12. Comparison of the Rankine/Von Mises composite yield contour with experimental data from Kupfer and Gerstle (1973).

platen is assumed to be rigid and has been modelled by vertically constraining the relevant nodes. The analyses have been carried out with a constrained Newton–Raphson iteration with line-searches (Feenstra, 1993; Schellekens, 1992).

The material which is considered is a concrete with a mean value of the compressive strength $f_{cm} = 35\,\text{MPa}$ and a maximum aggregate size $d_{\max} = 8\,\text{mm}$. On the basis of the CEB-FIP model code (CEB-FIP, 1990), the following material parameters have been estimated: Young's modulus $E_c = 32,710\,\text{MPa}$, Poisson ratio $\nu = 0.15$, tensile strength $f_t = 2.7\,\text{MPa}$, a tensile fracture energy $G_f = 0.06\,\text{N/mm}$ and a compressive fracture energy $G_c = 5.0\,\text{N/mm}$.

The load versus the displacement of the loading platen is depicted in Figure 14. Two different failure mechanisms can be distinguished. First, a splitting crack is formed at a load level of approximately $30\,\text{N/mm}^2$, which is attended with a reduction of the load. When the crack is fully developed the load starts to increase again, leading to a collapse mechanism which is governed by a compressive failure mode which consists of wedges which are pushed into the specimen, thereby further opening the existing splitting crack and separating the specimen into two parts. The final deformations are shown in Figure 15 for both meshes.

4.2. A DIRECT TENSION TEST

Similar to gradient damage models, one can define gradient plasticity models (de Borst and Mühlhaus, 1992; Pamin, 1994; de Borst and Pamin, 1996; de Borst and Pamin, 1996). For instance a gradient extension of the Rankine model would consist of

$$f = \sqrt{\tfrac{1}{2}\boldsymbol{\sigma}^T\mathbf{P}\boldsymbol{\sigma}} + \tfrac{1}{2}\boldsymbol{\pi}^T\boldsymbol{\sigma} - \bar{\sigma}(\kappa, \nabla^2\kappa) \tag{67}$$

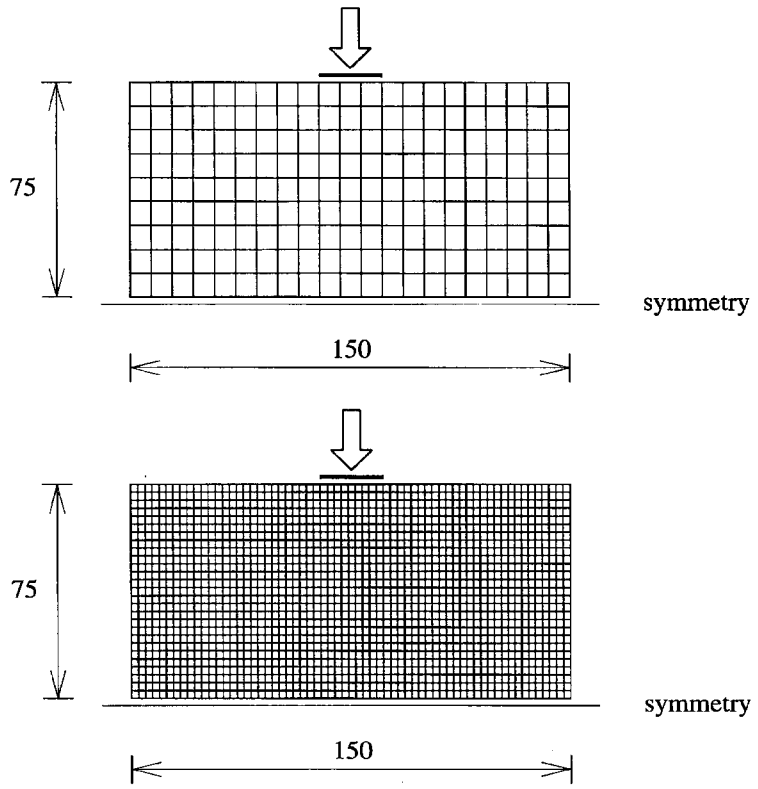

Figure 13. Finite element meshes for a cube splitting test. Each quadrilateral consists of four crossed triangles. Top: coarse mesh. Bottom: fine mesh.

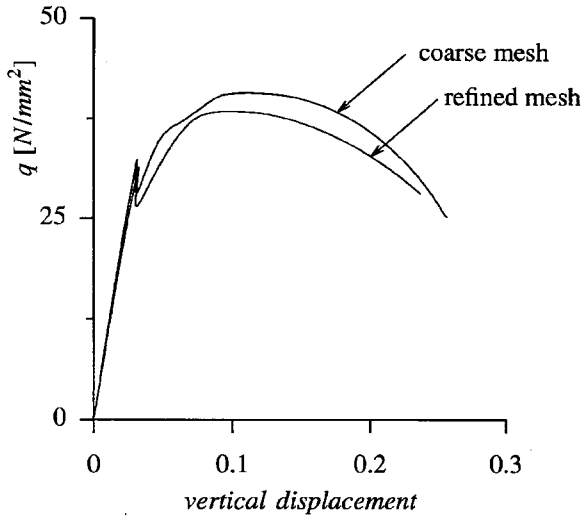

Figure 14. Load-deformation diagrams for a cube splitting test.

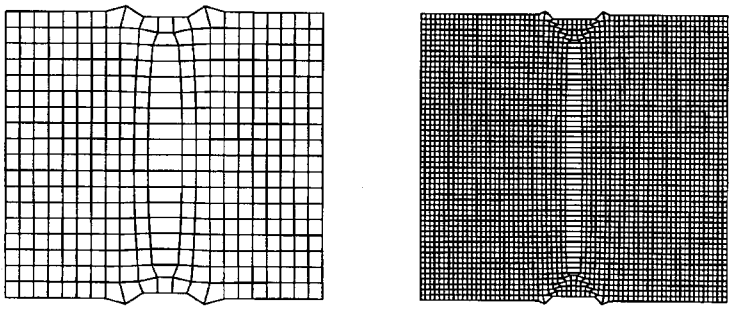

Figure 15. Deformations of the cube splitting test at final load level.

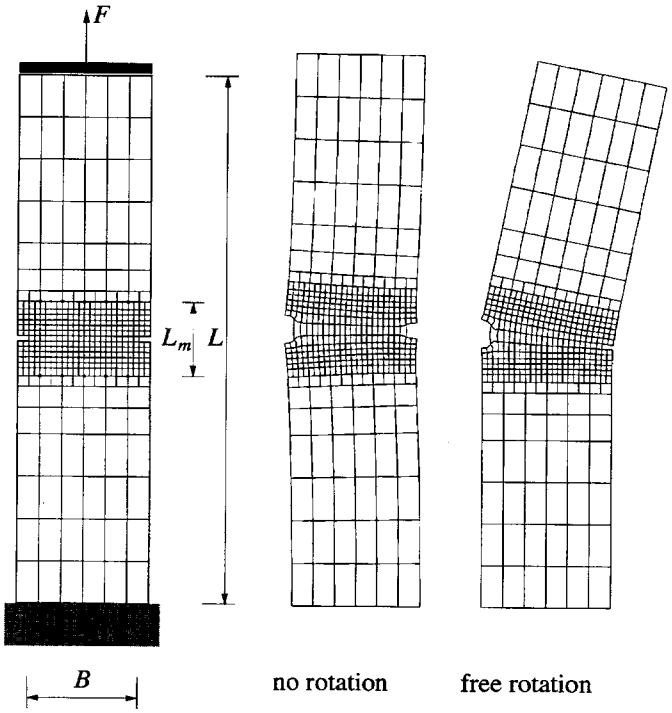

Figure 16. Direct tension test and deformed specimens according to gradient plasticity theory.

for the case of isotropic softening. When it is assumed that the dependence upon the gradient term is linear – the simplest possible case – then (67) reduces to

$$f = \sqrt{\tfrac{1}{2}\boldsymbol{\sigma}^T\mathbf{P}\boldsymbol{\sigma}} + \tfrac{1}{2}\boldsymbol{\pi}^T\boldsymbol{\sigma} - \bar{\sigma}(\kappa) - \bar{c}\nabla^2\kappa. \tag{68}$$

In the example calculations that will be presented below $\bar{c}$ has been taken proportional to the rate of softening, for which the proposal of Hordijk (1991) has been adopted, so that: $\bar{c} = l^2\partial\bar{\sigma}/\partial\kappa$, with l the internal length scale parameter, which sets the gradient influence.

The direct tension test has been performed on notched plain concrete specimens under deformation control (Hordijk, 1991), and has been analysed in Pamin (1994); Rots and de

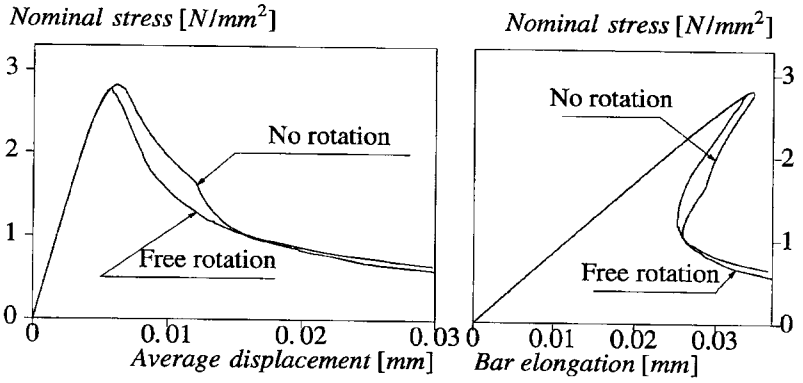

Figure 17. Load-displacement curves obtained using the gradient-enhanced model.

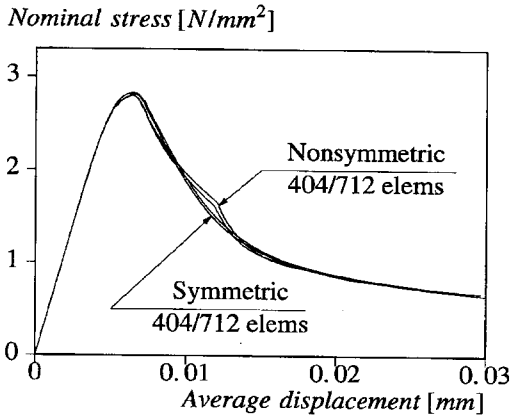

Figure 18. Mesh sensitivity of simulations using the gradient plasticity.

Borst (1989). The test configuration is shown in Figure 16. The material data for the used lightweight concrete are: $L = 250\,\text{mm}$, $B = 60\,\text{mm}$, thickness $t = 50\,\text{mm}$, Young's modulus $E = 18,000\,\text{MPa}$, tensile strength $f_t = 3.4\,\text{MPa}$, fracture energy $G_f = 0.0593\,\text{N/mm}$. The internal length scale l has been assumed equal to 2 mm. With the above experimental value for the fracture energy and employing Hordijk's (1991) equivalent tensile softening curve, an ultimate equivalent fracture strain $\kappa_u \approx 7.14{\cdot}10^{-3}$ is then computed. The Possion ratio ν was taken equal to zero. The specimen is fixed at the bottom and tied to a rigid plate at the top. A rotational spring, modelling the stiffness of the testing rig, is included to counteract the rotation of the upper plate. The average deformations are measured over a base $L_m = 35\,\text{mm}$ according to the original position of five extensometers.

Figure 16 presents the deformations of the specimen for two cases: (i) the rotation of the upper edge is prevented by a rotational spring with a stiffness $k_r = 10^9\,\text{Nmm/rad}$ and (ii) assuming free rotation of the upper end of the specimen ($k_r = 0$). The left part of Figure 17 presents a relation between the nominal stress $\sigma_N = P/(tB)$ and the average displacement over the measuring length L_m. The right part of the figure shows the nominal stress plotted as a function of the vertical displacement of the upper edge. A clear snap-back

behaviour is observed, which is caused by the elastic unloading outside the fracture zone. This demonstrates the necessity of a careful choice of the degrees-of-freedom for the loading control in the experiment and the advantage of using the indirect displacement control in numerical simulations of localisation phenomena (Feenstra, 1993; de Borst, 1986; Schellekens, 1992).

For both cases the specimen exhibits flexing to one side starting at the peak load. In the absence of a rotational constraint the further deformations remain nonsymmetric. When a rotational stiffness is included in the model, the nonsymmetric stage of fracture development is followed by a symmetric failure mode and the return to the symmetric mode corresponds to a 'bump' in the load-displacement curves (Figure 17). This nonsymmetric deformation pattern has also been observed in the experiments (Hordijk; 1991) and is consistent with analytical arguments (Bažant and Cedolin, 1993).

The response of the model that includes a rotational stiffness is similar to the results obtained for the smeared-crack model, although in the latter case the fracture localises (of course) in just one row of elements (Rots and de Borst, 1993). Another striking observation is that the calculation with the gradient-enhanced continuum is almost not hampered by spurious mechanisms of elements. The phenomenon frequently occurs in classical smeared-crack models and tends to destroy a proper convergence of the equilibrium-finding iterative procedure (de Borst and Rots, 1989).

We shall further analyse the case which includes the rotational stiffness of the test rig. Figure 18 compares load-displacement diagrams of the specimen with a diagram obtained in a simulation, in which symmetry has been enforced during the entire fracture process. This figure also shows that the gradient enhancement indeed virtually eliminates the mesh sensitivity, since the differences between the results of the various discretisations remain well in the margin that is normally accepted in case of mesh refinement.

The decrease of the load-carrying capacity and of the ductility in the post-peak regime with the increase of the structural size is characteristic for fracturing specimens. The load-displacement diagram in Figure 19 shows relations between the nominal stress and the average strain, defined as the average displacement divided by the measuring length L_m, obtained numerically for three specimens scaled uniformly. A *size effect* is obtained for the peak stress as well as for the ductility. This reproduction of the size effect is possible because of the introduction of an internal length scale $l = 2\,\text{mm}$, which sets the width of the fracture band ($w \approx 12.6\,\text{mm}$), and is independent of the specimen size (de Borst and Mühlhaus, 1992; de Borst and Pamin, 1996).

4.3. A DOUBLE-EDGE-NOTCHED SPECIMEN

Figure 20 shows the configuration of a double-edge-notched mixed-mode concrete fracture test (Nooru-Mohamed, 1992). The double-edge-notched specimen has been placed in a special loading frame that allowed for the investigation of various loading paths of combined shear and tension under force or deformation control.

Three specimen sizes ($L \times L$) have been investigated in the experiments: $200 \times 200, 100 \times 100, 50 \times 50\,\text{mm}$. The sizes of symmetrical notches were $25 \times 5, 12.5 \times 5$ and $6.25 \times 5\,\text{mm}$, respectively. The specimen thickness was $t = 50\,\text{mm}$ for all cases. The specimen was supported at the bottom and along the right-hand side below the notch. The shear force P_s was applied through the frame above the notch along the left-hand side of the specimen and the tensile force P was applied at the top. The frames were glued to the specimen. The relative shear deformation between the upper and lower half of the specimen δ_s was measured at the

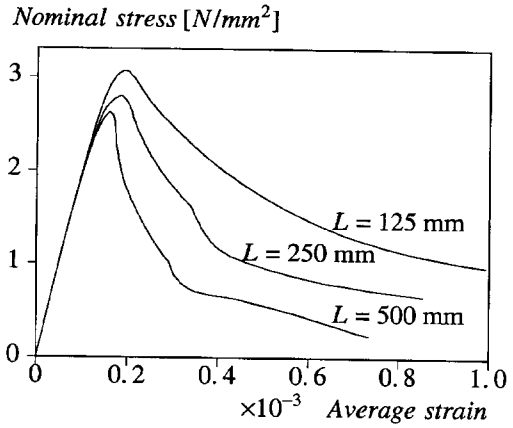

Figure 19. Size effect: load-displacement diagrams for three different sizes.

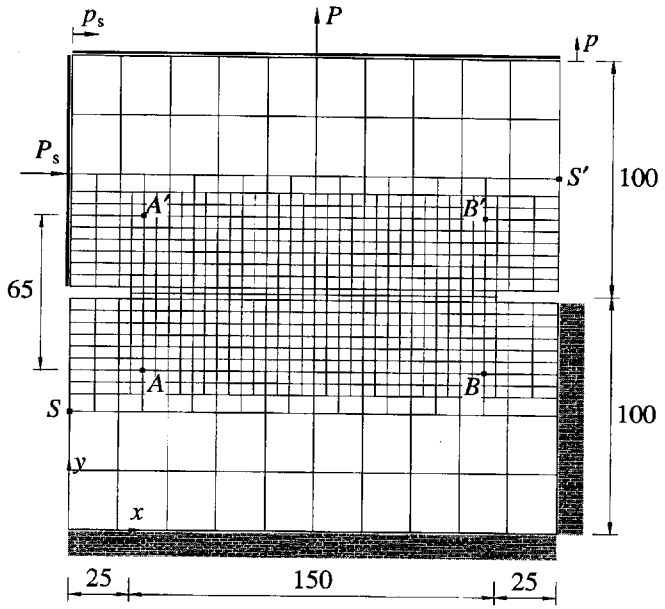

Figure 20. Geometry and discretisation for DEN-specimen tested by Nooru-Mohamed (1992).

points S and S′ on both sides and the relative normal deformation in the fracture zone δ was measured between the points A and A′ as well as between B and B′ and averaged. Owing to the servo-controlled system the loading could also be controlled by the deformations δ_s and δ.

Below we shall describe the simulations for loading path 4 of the experimental series using Rankine gradient-dependent plasticity (Pamin, 1994; de Borst and Pamin, 1996a; de Borst and Pamin, 1996b). In this series the largest specimen is used. The shear force is applied under force control and then kept constant while the normal loading is imposed under deformation control of δ. The material data used in numerical simulations are as follows: Young's modulus

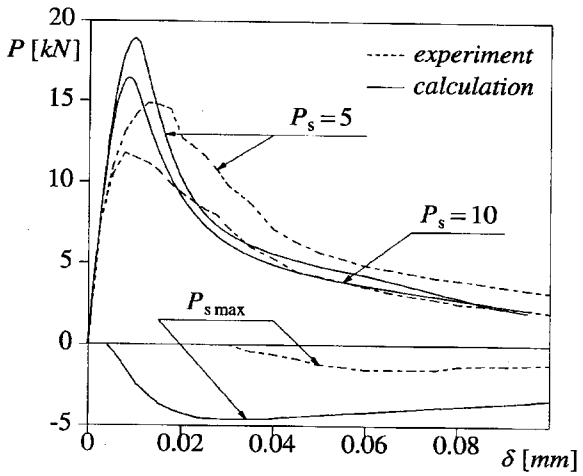

Figure 21. Tensile force vs average normal displacement for DEN-specimen (Nooru-Mohamed, 1992).

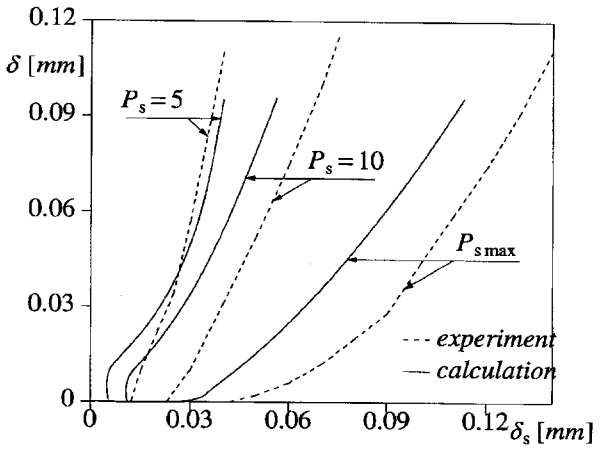

Figure 22. Average normal displacement vs average shear displacement for DEN-specimen.

$E = 30,000\,\mathrm{N/mm^2}$, Poisson's ratio $\nu = 0$, tensile strength $f_t \approx 3.0\,\mathrm{N/mm^2}$, fracture energy $G_f = 0.10\,\mathrm{N/mm}$. The nonlinear softening rule of Hordijk has again been employed. Unless stated otherwise, the internal length scale $l = 2\,\mathrm{mm}$ is assumed, so that $\kappa_u = 0.0136$.

Figures 21 and 22 show the experimentally determined and numerically simulated relations (Pamin, 1994; de Borst and Pamin, 1996a) between the tensile load P and the normal displacement δ and between δ and the shear displacement δ_s. The calculated maximum shear load $P_{s,\max} = 29.7\,\mathrm{kN}$ is larger than the experimental value (about 27.5 kN) and the ultimate load carrying capacity under subsequent tension is overestimated even more markedly. This is attributed to stress locking in the notch area and the ensuing overestimation of the stress in the presence of the lateral compression. On the other hand, the Rankine gradient plasticity model reproduces correctly the character of the experimental curves and is close to experiments for progressive softening.

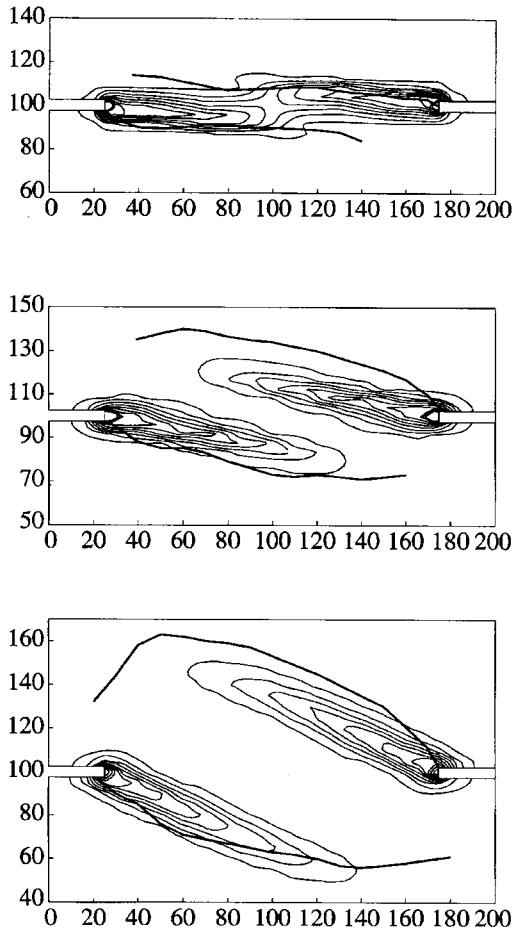

Figure 23. Contour plots of equivalent fracture strain and crack pattern (Nooru-Mohamed, 1992).

The simulated fracture process zones are compared with the average of the experimental crack locations at the front and back of the specimen in Figure 23. The agreement is reasonable and no bias of the mesh lines has been found (Pamin, 1994; de Borst and Pamin, 1996a) as was the case in simulations with the standard fixed smeared-crack concept (Nooru-Mohamed, 1992). For the case $P_s = 5\,\text{kN}$ the two fracture zones evolving from the notches finally join, for the other cases the width of the compressive strut is estimated correctly. The width of the fracture zones corresponds well to the analytical value $w = 2\pi l \approx 12.6\,\text{mm}$ (de Borst and Mühlhaus, 1992; de Borst and Pamin, 1996a). Unfortunately, the curved character of the cracks could not be simulated. Since this observation seems to be a general tendency in smeared simulations, it requires more investigation in the future. This holds *a fortiori* since lattice type models can represent the curved nature of cracks in concrete quite well (van Mier et al. 1994; Schlangen, 1993).

Acknowledgements

Many of the results discussed in this paper have come out of the doctoral research of P.H. Feenstra, J. Pamin, R.H.J. Peerlings and L.J. Sluys, and full information can be found in their dissertations and publications listed in the References.

References

Aifantis, E.C. (1984). On the microstuctural original of certain inelastic models, *Journal of Engineering Materials and Technology* **106**, 326–334.

Barenblatt, G.I. (1962). The mathematical theory of equilibrium cracks in brittle fracture, *Advances in Applied Mechanics* **7**, 55–129.

Bažant, Z.P. (1976). Instability, ductility and size effect in strain softening concrete, *ASCE Journal of Engineering Mechanics Division* **102**, 331–144.

Bažant, Z.P. (1983). Comment on orthotropic models for concrete and geomaterials, *ASCE Journal of Engineering Mechanics Division* **109**, 849–865.

Bažant, Z.P., Belytschko, T.B. and Chang, T.-P. (1984). Continuum model for strain-softening, *ASCE Journal of the Engineering Mechanics Division* **110**, 1666–1692.

Bažant, Z.P and Cedolin, L. (1993). Why direct tension test specimens break flexing to one side, *ASCE Journal of Structural Engineering* **119**, 1101–1113.

Bažant Z.P. and Oh, B. (1983). Crack band theory for fracture of concrete, *RILEM Materials and Structures* **16**, 155–177.

de Borst, R. (1986). *Nonlinear Analysis of Frictional Materials.* Dissertation, Delft University of Technology, Delft.

de Borst, R. (1987). Smeared cracking, plasticity, creep and thermal loading – a unified approach, *Computer Methods in Applied Mechanics and Engineering* **62**, 89–110.

de Borst, R. (1991). Simulation of strain localisation: A reappraisal of the Cosserat continuum, *Engineering Computations* **8**, 317– 332.

de Borst, R. (1993). A generalisation of J_2-flow theory for polar continua, *Computer Methods in Applied Mechanics and Engineering* **103**, 347–362.

de Borst, R., Benallal, A. and Peerlings R.H.J. (1997). On gradient-enhanced damage theories, *IUTAM Symposium on Granular and Porous Materials*, Kluwer, Dordrecht, in press.

de Borst, R. and Mühlhaus, H.B. (1992). Gradient-dependent plasticity: formulation and algorithmic aspects, *International Journal for Numerical Methods in Engineering* **35**, 521–539.

de Borst, R. and Nauta, P. (1985). Non-orthogonal cracks in a smeared finite element model, *Engineering Computations* **2**, 35–46.

de Borst, R. and Pamin, J. (1996a). Gradient plasticity in numerical simulation of concrete cracking, *European Journal of Mechanics: A/Solids* **15**, 295–320.

de Borst, R. and Pamin, J. (1996b). Some novel developments in finite element procedures for gradient-dependent plasticity, *International Journal for Numerical Methods in Engineering* **39**, 2477–2505.

de Borst, R. and Rots, J.G. (1989). Occurrence of spurious mechanisms in computations of strain-softening solids, *Engineering Computations* **6**, 272–280.

de Borst, R., Sluys, L.J., Mühlhaus, H.-B. and Pamin, J. (1993). Fundamental issues in finite element analysis of localisation of deformation, *Engineering Computations* **10**, 99–122.

Carmeliet, J. and de Borst, R. (1995). Stochastic approaches for damage evolution in standard and non-standard continua, *International Journal of Solids and Structures* **32**, 1149–1160.

Carter, B.J., Ingraffea, A.R. and Bittencourt, T.N. (1995). Topology-controlled modelling of linear and nonlinear 3D crack propagation in geomaterials, *Fracture of Brittle, Disordered Materials*, E & FN Spon, London 301–318.

CEB-FIP, *Model code 1990*, Bulletin d'Information, Lausanne (1990).

Cedolin, L. and Bažant, Z.P. (1980). Effect of finite element choice in blunt crack band analysis, *Computer Methods in Applied Mechanics and Engineering* **24**, 305–316.

Cope, R.J., Rao, P.V., Clark, L.A. and Norris, P. (1980). Modelling of reinforced concrete behaviour for finite element analysis of bridge slabs, *Numerical Methods for Non-Linear Problems*, Pineridge Press, Swansea, Vol. 1. 457–470.

Crisfield, M.A. (1982). Local instabilities in the nonlinear analysis of reinforced concrete beams and slabs, *Proceedings, Institute of Civil Engineers on Part 2* **73**, 135–145.

Crisfield, M.A. and Wills, J. (1989). Analysis of R/C panels using different concrete models, *ASCE Journal of Engineering Mechanics* **115**, 578–597.

Dugdale, D.S. (1960). Yielding of steel sheets containing slits, *Journal of the Mechanics and Physics of Solids* **8**, 100–108.
Feenstra, P.H. (1993). *Computational Aspects of Biaxial Stress in Plain and Reinforced Concrete*, Dissertation, Delft University of Technology, Delft.
Feenstra, P.H. and de Borst, R. (1995). A plasticity model for mode-I cracking in concrete, *International Journal for Numerical Methods in Engineering* **38**, 2509–2529.
Feenstra, P.H. and de Borst, R. (1996). A composite plasticity model for concrete, *International Journal of Solids and Structures* **33**, 707–730.
Herrmann, H.J., Hansen, H. and Roux, S. (1989). Fracture of disordered, elastic lattices in two dimensions, *Physical Review B* **39**, 637–648.
Hillerborg, A., Modeer, M. and Petersson, P.E. (1976). Analysis of crack formation and crack growth in concrete by means of fracture mechanics and finite elements, *Cement and Concrete Research* **6**, 773–782.
Hordijk, D.A. (1991). *Local Approach to Fatigue of Concrete*, Dissertation, Delft University of Technology, Delft.
Hrennikoff, A. (1941). Solution of problems of elasticity by the framework method, *Journal of Applied Mechanics* **12**, 169–175.
Ingraffea, A.R. and Saouma, V. (1985). Numerical modelling of discrete crack propagation in reinforced and plain concrete, *Fracture Mechanics of Concrete*, Martinus Nijhoff Publishers, Dordrecht, 171–225.
Kupfer, H.B. and Gestle, K.H. (1973). Behaviour of concrete under biaxial stresses, *ASCE Journal of Engineering Mechanics Division* **99**, 853–866.
Lasry, D. and Belytschko, T.B. (1988). Localization limiters in transient problems, *International Journal of Solids and Structures* **24**, 581–597.
Lemaitre, J. and Chaboche, J.L. (1990). *Mechanics of Solid Materials*, Cambridge University Press, Cambridge.
Mazars, J. (1984). *Application de la Mécanique de l'Endommagement au Comportement non Linéare et à la Rupture du Béton de Structure*, These d'Etat, Université Paris VI, Paris.
Mazars, J. and Pijaudier-Cabot, G. (1989). Continuum damage theory – application to concrete, *ASCE Journal of Engineering Mechanics* **115**, 345–365.
van Mier, J.G.M. (1991). Mode-I fracture of concrete: discontinuous crack growth and crack interface grain bridging, *Cement and Concrete Research* **21**, 1–15.
van Mier, J.G.M., Vervuurt, A. and Schlangen, E. (1994). Boundary and size effects in uniaxial tensile tests: a numerical and experimental study, *Fracture and Damage in Quasibrittle Structures*, E & FN Spon, London, 289–302.
Mühlhaus, H.-B. and Aifantis, E.C. (1991). A variational principle for gradient plasticity, *International Journal of Solids and Structures* **28**, 845–858.
Mühlhaus, H.-B. and Vardoulakis, I. (1987). The thickness of shear bands in granular materials, *Geotechnique* **37**, 271–283.
Ngo, D. and Scordelis, A.C. (1967). Finite element analysis of reinforced concrete beams, *Journal of the American Concrete Institute* **67**, 152–163.
Nooru-Mohamed, M.B. (1992). *Mixed-Mode Fracture of Concrete: an Experimental Approach*, Dissertation, Delft University of Technology, Delft.
Pamin, J. (1994). *Gradient-Dependent Plasticity in Numerical Simulation of Localization Phenomena*, Dissertation, Delft University of Technology, Delft.
Peerlings, R.H.J., de Borst, R., Brekelmans, W.A.M. and de Vree, J.H.P. (1996). Gradient-enhanced damage for quasi-brittle materials, *International Journal for Numerical Methods in Engineering* **39**, 3391–3403.
Pijaudier-Cabot, G. and Bažant, Z.P. (1987). Nonlocal damage theory, *ASCE Journal of the Engineering Mechanics* **113**, 1512–1533.
Rashid, Y.R. (1968). Analysis of prestressed concrete pressure vessels, *Nuclear Engineering and Design* **7**, 334–344.
Rots, J.G. (1988). *Computational Modeling of Concrete Fracture*, Dissertation, Delft University of Technology, Delft.
Rots, J.G. and de Borst, R. (1989). Analysis of concrete fracture in 'direct' tension, *International Journal of Solids and Structures* **25**, 1381–1394.
Schellekens, J.C.J. (1992). *Computational Strategies for Composite Structures*, Dissertation, Delft University of Technology, Delft.
Schlangen, E. (1993). *Experimental and Numerical Analysis of Fracture Processes in Concrete*, Dissertation, Delft University of Technology, Delft.
Schreyer, H.L. and Chen, Z. (1986). One-dimensional softening with localization, *ASME Journal of Applied Mechanics* **53**, 791–979.
Sluys, L.J. (1992). *Wave Propagation, Localisation and Dispersion in Softening Solids*, Dissertation, Delft University of Technology, Delft.

Sluys, L.J. and de Borst, R. (1996). Failure in plain and reinforced concrete – An analysis of crack width and crack spacing, *International Journal of Solids and Structures* **33**, 3257–3276.

Suidan, M. and Schnobrich, W.C. (1973). Finite element analysis of reinforced concrete, *ASCE Journal of the Structures Division* **99**, 2109–2122.

Vecchio, F.J. and Collins, M.P. (1982). *The Response of Reinforced Concrete to in-Plane Shear and Normal Stresses*, Publication 82-03, University of Toronto, Toronto.

Vonk, R. (1992). *Softening of Concrete Loaded in Compression*, Dissertation, Eindhoven University of Technology, Eindhoven.

Willam, K., Pramono, E. and Sture, S. (1986). Fundamental issues of smeared crack models, *Proceedings SEM/RILEM International Conference on Fracture of Concrete and Rock* 142–157.